Research Square

Preprints are preliminary reports that have not undergone peer review.
They should not be considered conclusive, used to inform clinical practice,
or referenced by the media as validated information.

Disentangling the dynamic and thermal effects of the Tibetan Plateau on the amplitude of ENSO

Baohuang Su

subh@cma.gov.cn

China Academy of Meteorological Sciences https://orcid.org/0009-0008-9086-7754

Yong Sun

Institute of Tibetan Plateau Research Chinese Academy of Sciences

Shuangze Han

China Academy of Meteorological Sciences

Na Wang

UC Santa Barbara: University of California Santa Barbara

Research Article

Keywords: Tibetan Plateau, ENSO amplitude, dynamic effect, thermal effect, Bjerknes index, air-sea coupling, Walker circulation

Posted Date: October 27th, 2026

DOI: https://doi.org/10.21203/rs.3.rs-10586960/v1

License: This work is licensed under a Creative Commons Attribution 4.0 International License.
Read Full License

Disentangling the dynamic and thermal effects of the Tibetan Plateau on the amplitude of ENSO

Baohuang Su[1,4*], Yong Sun[2], Shuangze Han[1,4], Na Wang[3]

[1] Institute of Tibetan Plateau Meteorology, Chinese Academy of Meteorological Sciences, Beijing 100081, China

[2] State Key Laboratory of Tibetan Plateau Earth System, Environment and Resources (TPESER), Institute of Tibetan Plateau Research, Chinese Academy of Sciences, Beijing, 100101, China

[3] University of California, Santa Barbara, Santa Barbara, CA 93106, USA

[4] Heavy Rain and Drought-Flood Disasters in Plateau and Basin Key Laboratory of Sichuan Province, Institute of Tibetan Plateau Meteorology, China Meteorological Administration, Chengdu, 610213, China

*Corresponding author: subh@cma.gov.cn

Abstract: This study investigates the impact of the Tibetan Plateau (TP) on El Niño-Southern Oscillation (ENSO) amplitude based on three long-term numerical experiments using the Community Earth System Model (CESM). Results indicate that the TP significantly suppresses the ENSO amplitude by 0.51 °C (−41%), where the dynamic effect (DY) and thermal effect (SH) of the TP exert opposite influences, contributing to a reduction of 0.58 °C (−46%) and an increase of 0.07 °C (5%), respectively. Analysis of the Bjerknes coupled stability index reveals that the combined DY+SH effects lower the index, which is dynamically consistent with the weakened ENSO amplitude. This reduction is primarily manifested through the enhancement of mean advection feedback, the weakening of thermocline feedback, Ekman feedback, and zonal advective feedback, as well as the reduction of thermodynamic damping feedback, thereby regulating the ENSO growth rate. In each feedback process, the influence of DY consistently dominates and acts in the opposite direction to SH. Specifically, the weakening of the thermocline, Ekman, and zonal advective feedbacks is closely linked to a deepened thermocline and reduced sensitivity of vertical and zonal ocean currents to atmospheric forcing, while the reduction in thermodynamic damping feedback is attributed to the enhancement of shortwave radiation feedback driven by a strengthened Walker circulation. This study provides a mechanistic basis for how the TP modulates ENSO through air-sea coupling processes, offering valuable insights for improving ENSO predictability.

Keywords: Tibetan Plateau, ENSO amplitude, dynamic effect, thermal effect, Bjerknes index, air-sea coupling, Walker circulation.

1. Introduction

The uplift of the Tibetan Plateau (TP) is one of the most significant geological events of the Cenozoic era, exerting profound dynamic and thermal influences on global climate evolution (Harrison et al., 1992; Molnar et al., 2010; Huang et al., 2023). Its thermal effect impact surrounding airflows through increased sensible and latent heat release, shaping the formation and development of the Asian summer monsoon. Simultaneously, TP's topography significantly influences atmospheric circulation patterns by blocking westerlies and driving tropical monsoons. Despite different perspectives on the primary factors influencing the formation of the South Asian monsoon, Boos and Kuang (2010) highlight the isolating effect of the Himalayas, while Wu G et al. (2012) consider the thermal effects of the TP as the main mechanism for monsoon intensification; the relative importance of these roles requires further evaluation. Enhancing our grasp of how the TP's dynamic and thermal roles evolve and interact with climate change is essential for fully comprehending the intricate dynamics of long-term climatic shifts (Hu and Duan, 2015; Duan et al., 2024).

The interaction between the TP and ENSO (El Niño-Southern Oscillation) is a topic of great interest in climatology. Theoretical and numerical simulation studies indicate that the presence of global mountain ranges plays a key role in anchoring the subtropical atmospheric teleconnection propagation pathways triggered by the heating associated with El Niño events (Blackmon et al., 1987; DeWeaver and Nigam, 1995; Nigam and DeWeaver, 1998). TP exerts a pronounced modulation on the impact of ENSO events on the Asian monsoon, with its dynamic and thermal properties

representing a pivotal factor in the interannual variability of the monsoon during El Niño and La Niña periods (Wu and Ni, 1997; Krishnan et al., 1998). Regional snow anomalies on the TP that alter thermal conditions may also influence ENSO teleconnection processes and modulate the Asian monsoon circulation (Shaman and Tziperman, 2005; Wu et al., 2012).

Furthermore, fluctuations in the TP's thermal conditions, including potential alterations in albedo, may precipitate the formation of anomalous trade winds in the equatorial Pacific, subsequently facilitating the development of ENSO (Chen et al., 2001; Nan et al., 2009; Zhou et al., 2009). Numerical experiments based on a general circulation model (GCM) reveal that thermal condition changes over the TP are one of the key processes that trigger stronger El Niño events (Barnett et al., 1989). Specifically, the surface darkening of the Tibetan Plateau (TP) acts as a pivotal teleconnection hub that intensifies the tropical Pacific zonal temperature gradient and modulates equatorial climate patterns via remote air-sea interactions (Tang et al., 2025). Abnormal surface heating caused by wind speed anomalies over the TP in spring is closely linked to the occurrence of subsequent winter ENSO events, as it affects the meridional monsoon circulation between the Indian and Pacific Oceans and the air-sea interaction in the North Pacific, thereby inducing ENSO events (Yu et al., 2022). Numerical experiments have demonstrated that the TP exerts a substantial influence on the large-scale circulations of the tropical Pacific, specifically the trade winds, via its dynamic or thermal climate effects. This consequently contributes to the maintenance of ENSO activity (Kitoh, 2007; Naiman et al., 2017; Wen et al., 2020).

The synthesis of the aforementioned research indicates that the TP exerts a considerable influence on the sea-air interactive system over the tropical Pacific, primarily through its dynamic and thermal processes. While several studies have addressed this topic, the mechanisms by which the TP's dynamic and thermal forcing and related physical processes or feedbacks contribute to ENSO activity remain unclear, underscoring the need for further in-depth research. The objective of this study is to explicitly identify and isolate the specific impacts of the TP's dynamic and thermal roles on tropical ENSO activity.

In light of the above scientific issues, this study employs a fully coupled atmosphere-ocean model to perform three long-term integrated numerical experiments under the modern climate background to investigate the role of the TP in the climate system, in particular its potential impact on the tropical ENSO phenomenon. The following sections sequentially describe the model, experimental setup, and analysis methods (Section 2); present the main results, including the response of the tropical Pacific climate mean state to the dynamic and thermal effects of the TP, such as sea surface temperature (SST), atmospheric circulation, and ocean circulation (Section 3); provide potential mechanisms discussed based on the Bjerknes feedback analysis method (Section 4); and summarize the research findings (Section 5).

2. Model and experimental designs

2.1. Model description

In this study, we used the Community Earth System Model (CESM version 1.2.2) released by the National Center for Atmospheric Research (NCAR) (Hurrell et al.,

2013). The atmospheric component (CAM4) of this model has a horizontal grid spacing of 3.75° × 3.75° and 26 hybrid vertical coordinates. The ocean component (POP2) uses a tripolar grid with a polar horizontal grid spacing of approximately 3° and 1° near the equator, with 60 vertical layers. The sea ice (CSIM) and land (CLM4) components use the same grid as POP2 and CAM4. Given the requirement for long-term integration, we chose a lower resolution configuration to reduce the cost of computing. The low-resolution version of CESM effectively simulates the spatial and temporal characteristics of ENSO, especially in the low-frequency band, where the ENSO spectrum contains more energy and is closer to observations (Shields et al., 2012).

2.2. Experimental designs

In this study, we designed three sets of experiments to investigate the role of TP sensible heat and topography on ENSO: a pre-industrial control experiment (CMP), an experiment without TP (CNP), and an experiment without TP's surface sensible heat (NSH). The CMP and CNP experiments are based on the work of Su et al. (2018), and the specific design is detailed in that literature. The CMP experiment uses modern TP and pre-industrial greenhouse gas concentrations, combined with modern land-sea distribution for numerical simulation. The CNP experiment has the same configuration as CMP, but removes the topographical features of the TP, adjusting areas with topography higher than 300 metres to 300 metres (Figure 1b). The NSH experiment, following the method of He et al. (2020), retains the TP topography of CMP, but turns off the surface sensible heat forcing in this region (Figure 1a, blue line).

We used the same approach as He et al. (2020) to disentangle the independent

effects of the TP's sensible heat and topography on the ENSO. Specifically, by comparing the results of CMP with CNP, we assessed the combined effects of the thermal and dynamical effects of the TP on ENSO, while comparisons between CMP and NSH, and NSH and CNP, allowed us to quantify the respective contributions of sensible heat and topographic dynamical effects. In the subsequent text, we abbreviate the dynamic and thermal effects of the TP, the dynamic effect alone, and the thermal effect alone as DY+SH, DY, and SH, respectively.

To ensure the climate system reached a full quasi-equilibrium state and to establish a reliable climate baseline, ultra-long numerical integrations were conducted for all three experiments. The CMP experiment was extended to a total of 3800 model years based on its original integration. The CNP and NSH experiments were branched from the same point (the 1100th model year of CMP) and each independently integrated for 3800 years, bringing the total duration of all three experiments to 3800 years. As illustrated in Fig. 1c–d, the time series of global annual mean 2-meter air temperature and upper ocean temperature at 1 km depth exhibit high stability after long-term integration, with no significant monotonic trends, indicating that the deep ocean has achieved a quasi-equilibrium state. Meanwhile, the Atlantic Meridional Overturning Circulation (AMOC) index (Fig. 1e) shows that the CMP remains stable at approximately 18 Sv, while the AMOC in the CNP and NSH experiments rapidly adjusted and stabilized at lower magnitudes following the removal of TP topography. Furthermore, Fig. 1f presents the 200-year running standard deviation of the Niño 3.4 index. The results demonstrate that despite some centennial-scale internal fluctuations,

the fluctuation amplitude near the equilibrium state is minimal (approximately 0.02°C). This confirms that the selected analysis period has entered a statistically stationary phase, eliminating potential interference from the spin-up process on amplitude assessment and allowing for an accurate reflection of ENSO dynamical characteristics under these climatic backgrounds.

2.3. BJ index

To understand how the characteristics of ENSO are altered, we adopted the BJ coupled stability index formulated by Jin et al. (2006) to evaluate the strength of large-scale ENSO.

$$\mathrm{R} = -\left[a_1 \frac{\langle \Delta\bar{u} \rangle_E}{L_x} + a_2 \frac{\langle \Delta\bar{v} \rangle_E}{L_y}\right] - \alpha_s + \mu_a \beta_u \langle -\frac{\partial \bar{T}}{\partial x} \rangle_E + \mu_a \beta_h \langle \frac{\bar{w}}{H_1} \rangle_E \alpha_h + \mu_a \beta_w \langle -\frac{\partial \bar{T}}{\partial z} \rangle_E \quad (1)$$

The first two negative terms represent the mean advection feedback, the third negative term represents the thermodynamic damping, and the subsequent three positive terms represent the effects of the zonal advective feedback, thermocline feedback, and Ekman feedback, respectively. These coefficients are computed from approximated balance equations.

$$\langle Q \rangle_E = -\alpha_s \langle T \rangle_E$$

$$[\tau_x] = \mu_a \langle T \rangle_E$$

$$\langle h \rangle_E - \langle h \rangle_W = \beta_h [\tau_x]$$

$$\langle H_w(\bar{w}) w \rangle_E = -\beta_w \langle \tau_x \rangle$$

$$\langle u \rangle_E = \beta_u [\tau_x]$$

$$\langle H(\overline{w})T_{sub}\rangle_E = \alpha_h\langle h\rangle_E$$

Here, E and W denote two regions defined by distinct SST response characteristics: the central and eastern equatorial Pacific (E; 180–90°W, 5°N–5°S) and the western equatorial Pacific (W; 120°E–180°, 5°N–5°S). $\mathcal{Q}$ is the net downward heat flux, τ_x is the equatorial trade wind anomaly, $\langle h\rangle_W$ is the thermocline depth in thewestern equatorial Pacific. $H_w(\overline{w})$ is a step function considering only climatological upwelling, and T_{sub} is the anomalous subsurface temperature. In these formulations, overbars denote the annual mean climatological state, while variables without overbars represent anomalies (deviations from the climatology). Specifically, $\overline{w}$ is the climatological mean vertical velocity, whereas w is the anomalous vertical velocity component. Similarly, $\overline{\mathrm{T}}$ and T represent the climatological mean and anomalous sea surface temperatures (SST), respectively. Other parameters are given in Table 1.

3. Simulated mean tropical climates and ENSO

3.1. Changes in ENSO amplitude

In the CMP experiment, the standard deviation (STD) of 2-7-year band-pass filtered sea surface temperature anomalies (SSTA) is primarily concentrated in the equatorial central and eastern Pacific (Figure 2a). The spatial distribution of the SSTA STD in the NSH experiment is similar to that of the CMP (Figure 2b). In the CNP experiment, the STD in the central and eastern Pacific is significantly higher than in the CMP and NSH, reaching up to 1°C (Figure 2c). Compared to the CNP, the STD over the entire tropical Pacific is significantly reduced in the CMP, especially in the equatorial central and eastern regions (Figure 2d), suggesting that the DY+SH effects

of the TP jointly diminish the interannual variability of SST. Further analysis reveals that the reduction in this variability is primarily driven by the dynamic (DY) effect of the TP (Fig. 2e), whereas the thermal (SH) effect exerts a marginal enhancing influence, although its overall contribution remains relatively weak (Fig. 2f).

To quantitatively assess the suppressing effect of the TP on ENSO activity, we calculated the STD of the Niño3.4 index, which is the averaged SSTA in the region from 170°W–120°W and 5°S–5°N. In the CMP experiment, the monthly STD of the Niño3.4 index is lower throughout the year compared to the CNP experiment (Figure 3a), with an annual mean reduction of 0.51 ℃ (approximately 41%). This indicates that the combined dynamic and thermal effects of the TP significantly suppress ENSO variability. Compared to the CNP, the monthly STD in the NSH experiment decreases by 0.58 ℃ (~46%) across all months (Fig. 3b). Conversely, the STD in CMP is slightly higher than that in NSH by approximately 0.07 ℃ (representing a ~5% increase relative to the annual mean STD of CNP), except during summer to early autumn (JJAS) (Fig. 3c). These findings suggest that the variations in ENSO amplitude are primarily modulated by the dynamic effect, while the contribution of the thermal effect remains relatively limited. Furthermore, the frequency of extreme SST anomalies is markedly higher in the CNP experiment (Fig. 3e), whereas the distribution patterns in NSH and CMP are fundamentally consistent (Fig. 3f).

Finally, we examined the periodic power spectral distribution of SSTAs in the three experiments. In the CNP experiment, spectral values show a systematic enhancement across all periods, particularly in the 2–7-year band, indicating robust

ENSO variability with concentrated energy across this broad range (Fig. 3g). In contrast, the power spectrum in the CMP experiment remains relatively flat within the 2–8-year period range; the spectral power is significantly suppressed without sharp peaks, illustrating that the presence of the TP leads to weakened ENSO amplitude, increased frequency, and greater irregularity. The NSH experiment shows a spectral distribution and intensity highly similar to those in CMP, further demonstrating that the contribution of sensible heat to ENSO spectral characteristics is weak (Fig. 3h, i). Consequently, the TP primarily suppresses ENSO variability and constrains its periodic distribution through topographic dynamical effects, while the impact of sensible heat remains relatively limited.

3.2. Response of the SST and atmospheric trade winds

The characteristics of El Niño phenomena are generally associated with changes in the background state, such as mean wind speed and thermocline depth (Fedorov and Philander, 2000; Manucharyan and Fedorov, 2014; Siuts et al., 2023). We investigated how the TP modifies the background climatic state of the tropical Pacific.

In the CMP experiment, the annual mean SST of the tropical Pacific is characterized by a warm pool in the western region and a cold tongue in the eastern region (Figure 4a), reflecting the combined impact of the mean trade winds and their associated oceanic upwelling processes on the SST (Figure 5a). The combined DY+SH effects lead to significant warming in the western equatorial Pacific and a slight intensification of the eastern cold tongue (Fig. 4d), indicating a weakened zonal SST gradient across the equator. The individual DY effect causes widespread cooling in the

central and eastern tropical Pacific, with a spatial distribution highly consistent with the SH+DY effect (Fig. 4e), demonstrating that this cooling is primarily driven by the DY effect (Figs. 5e, 5f). In contrast, the SH effect leads to warming north of the central and eastern equatorial Pacific and cooling to its south, which partially offsets the cooling effect induced by the DY effect.

The aforementioned SST variations induced by DY and SH are closely associated with changes in the equatorial trade wind system (Figs. 5e, 5f). Specifically, the DY effect strengthens the climatological North Pacific Subtropical High, leading to intensified trade winds (Fig. 5e), which subsequently promote SST cooling by enhancing evaporation and upwelling. The impact of the SH effect is nearly the opposite; particularly in the Northwest Pacific, negative pressure anomalies weaken the pre-existing high-pressure system, resulting in attenuated trade winds and slight warming in the equatorial region (Fig. 5f). The combined DY+SH effect induces an overall positive pressure anomaly over the North Pacific and strengthens the equatorial trade winds (Fig. 5d), triggering widespread SST cooling through the wind-evaporation-SST feedback process.

The Walker circulation serves as an indicator of the location of deep tropical atmospheric convection and plays a pivotal role in key air-sea coupling regions, which is critical for ENSO activity. Under the climatological mean state, the CMP experiment exhibits significant ascending motion over the western Pacific warm pool, while the central and eastern Pacific is dominated by descending motion (Figure 6a), forming a typical Walker circulation. The combined DY+SH effects of the TP strengthen this

circulation, manifested as enhanced ascending motion in the western Pacific and intensified descending motion in the eastern Pacific (Fig. 6d). The spatial distribution of anomalies induced by the individual DY effect is highly consistent with the SH+DY effect, indicating that the strengthening of the Walker circulation primarily stems from dynamical forcing (Fig. 6e). In contrast, the impact of the SH effect on the Walker circulation is more localized, with anomalous signals primarily concentrated in the central and western Pacific (Fig. 6f), reflecting the spatial limitation of thermal forcing in modulating the zonal circulation.

3.3. Response of the oceanic processes

In the tropical Pacific, the mean states of the oceanic circulation and thermodynamic conditions are significantly influenced by the TP (Figures 7 and 8). Anomalous changes in the trade winds are key to understanding the alterations in vertical temperature and ocean current distributions across the equatorial Pacific. The combined SH+DY effects strengthen the equatorial trade winds, thereby enhancing the westward surface flow and eastward subsurface flow (5°S–5°N) across the equatorial Pacific (Fig. 7d). Correspondingly, both the upwelling in the eastern Pacific and the downwelling in the western Pacific are intensified (Fig. 7d). Compared to the CNP experiment, the CMP simulation exhibits a deepened thermocline in the western Pacific, where eastward advection leads to warm water accumulation and increased upper-layer SST, while the eastern Pacific cools due to enhanced upwelling (Fig. 7c). These variations in the mixed-layer circulation and thermal conditions are primarily driven by the DY effect (Fig. 7e), whereas the SH effect, despite partially offsetting the dynamical

277 impact, remains relatively weak in magnitude (Fig. 7f).

278 The meridional structure of the upper ocean circulation responds dynamically to
279 the DY+SH effects of the TP, consistent with the anomalies in the mean near-surface
280 atmospheric circulation. Anomalous zonal winds triggered by the SH+DY effects
281 induce meridional Ekman transport anomalies, which subsequently evoke
282 compensatory downwelling in the subtropics by modulating the intensity of equatorial
283 upwelling, thereby weakening the climatological Pacific Subtropical Cells (STCs) (Fig.
284 8d). Under individual DY forcing, the response of the tropical upper meridional ocean
285 circulation and thermal structure is generally consistent with the SH+DY effects (Fig.
286 8e). In contrast, the SH effect acts in the opposite direction with a relatively weak
287 contribution (Fig. 8f), indicating that the adjustment of the tropical meridional ocean
288 circulation primarily responds to the dynamical forcing of the TP.

289 ## 4. Mechanisms

290 ### 4.1 The changes of the BJ index

291 Previous studies have indicated that estimates of ENSO growth rates derived from
292 the Bjerknes feedback index (BJ index) are generally consistent with those obtained
293 from the STD of SSTAs (Chen et al., 2019). Specifically, a more stable coupled ocean-
294 atmosphere system is unfavorable for ENSO growth, leading to a weakening of ENSO
295 amplitude. In this section, we examine the budget of the BJ index based on Equation
296 (1) to elucidate the relative impact of physical processes associated with the DY+SH
297 effects of the TP on the variation of ENSO amplitude.

298 Figure 9a illustrates that the simulated BJ index in the CMP experiment is a weak

negative value (−0.67 $year^{-1}$), indicating that under current climate conditions, ENSO behaves as a weakly damped oscillator. This is consistent with the qualitative results of observational data (e.g., Kim and Jin, 2011; Im et al., 2015; Ren and Liu, 2025). The main sources contributing to the negative BJ index are thermal damping and mean advection feedback, while thermocline feedback, zonal advective feedback, and Ekman feedback are the contributors that make the BJ index positive. Similarly, the main processes leading to ENSO being a weakly damped oscillation in the CNP and NSH simulations are broadly similar to those in the CMP experiment (Figure 9a).

Compared to the CNP experiment, the linear growth rate of ENSO (indicated by the BJ index) in the CMP experiment decreased by 0.50 $year^{-1}$ (Figure 9b), indicating that the combined thermal and dynamic effects of the TP suppress ENSO development. Within this dynamical framework, except for the thermodynamic damping (TD) term, which contributes −28.0%, all other feedback processes contribute positively to the reduction of the BJ index; specifically, the contributions from mean advection (MA), Ekman feedback (EK), thermocline feedback (TH), and zonal advective feedback (ZA) are 66.0%, 40.0%, 18.0%, and 4%, respectively. Further decomposition reveals that the dynamic (DY) and thermal (SH) effects of the TP exert opposite influences on the ENSO growth rate: the DY effect reduces it by −0.61 $year^{-1}$ (accounting for 53.3% of the total suppressing contribution), primarily by weakening the negative TD feedback and the positive MA feedback, while reducing the positive ZA, EK, and TH feedbacks. Conversely, the SH effect increases the growth rate by +0.11 $year^{-1}$ (representing a 46.7% offsetting contribution), mainly by enhancing the TD, ZA, and TH feedbacks, whereas

the changes in MA and EK processes are relatively small. Consequently, the net suppressing effect of the TP on the ENSO growth rate primarily stems from its dynamic effect.

Quantitative analysis of the BJ index demonstrates that the SH+DY effects of the TP reduce the BJ index, indicating a suppression of the ENSO growth rate, which is consistent with the conclusions in Section 3.1. Simultaneously, the DY and SH effects lead to a decrease and increase in the BJ index, respectively, corresponding to the reduction and enhancement of the Niño 3.4 STD (Fig. 3); this confirms that the variations in ENSO amplitude are consistent with the dynamical mechanisms reflected by the BJ index. To understand how the various feedback processes collectively result in the weakening of the BJ index, the changes in internal parameters within each feedback term will be analyzed in the following sections. Consequently, the net suppressing effect of the TP on the ENSO growth rate is primarily driven by its dynamical effect.

4.2 Analysis of mean advection feedback change

The combined DY+SH effects of the TP result in an enhancement the mean advection (MA) damping feedback by 0.33 $year^{-1}$, a change caused by the intensified mean zonal (+57.4%) and meridional (+38.4%) flow damping effects (Figure 9c). Specifically, the adjustments in the mean zonal flow are directly associated with the strengthened mean trade winds (Figure 5d), where the intensification of the trade winds over the tropical Pacific leads to a significant outflow near the equator and a mean easterly zonal flow within the oceanic mixed layer of the eastern Pacific (Fig. 7d).

Further analysis indicates that the variation in MA feedback is primarily dominated by the trade wind anomalies induced by the DY effect, accounting for a contribution of 112.0% (Fig. 9c); meanwhile, the SH effect mainly serves to weaken the MA feedback by modulating the meridional flow, with an influence of only 12.0% (Fig. 9c).

4.3 Change of zonal advective feedback

The variation in ZA feedback stems from three parameters: the equatorial mean SST gradient $\langle -\frac{\partial \bar{T}}{\partial x} \rangle_E$, the zonal flow response coefficient β_u, and the air-sea coupling coefficient μ_a (Table 1). Under the combined DY+SH effects of the TP, $\langle -\frac{\partial \bar{T}}{\partial x} \rangle_E$ is enhanced by 13.6% (Fig. 9c), corresponding to the transition from cold anomalies in the eastern Pacific to warm anomalies in the western Pacific (Fig. 4d), with the DY and SH effects contributing 10.0% and 3.2%, respectively. β_u decreased by 26.3% (Fig. 11d), reflecting a weakened response of the zonal flow to wind stress anomalies; specifically, the DY effect causes it to decrease by 33.7%, while the SH effect leads to an increase of 11.1% (Fig. 11e, f).

Secondly, the presence of the TP results in an general strengthening of the Pacific Walker circulation (Figure 6d), thereby modulating the sensitivity of the response of SSTAs to wind stress, μ_a. Specifically, μ_a is strengthened in the western equatorial Pacific and weakened in the eastern equatorial Pacific (Figure 10d), which is consistent with the dynamical process where enhanced ascending convective activity in the western Pacific helps maintain warm SSTs, while intensified descending motion in the eastern Pacific suppresses SST rise. Comparing Figures 10d and 10e, it is evident that the spatial variation of μ_a primarily stems from the DY effect of the TP, which

increases the east-west regionally averaged μ_a by 6.5% (Figure 9c). The SH effect leads to a 9.5% increase in the regionally averaged μ_a (Figure 9c), showing an overall increasing trend across the tropical Pacific except for a slight decrease in the central Pacific (180°–150°W) (Figure 10f). Consequently, the magnitudes of the impact of the TP's DY and SH effects on μ_a are roughly comparable.

In summary, although $\langle -\frac{\partial \bar{T}}{\partial x} \rangle_E$ and μ_a make positive contributions, the reduction in β_u remains the dominant factor in the weakening of the ZA feedback, resulting in a reduction of 0.02 year^{-1}, which accounts for approximately 4.0% of the total decrease in the BJ index. The DY and SH effects offset each other within this feedback, leading to a decrease of 0.19 year^{-1} and an increase of 0.17 year^{-1} in the BJ index, respectively.

4.4 Analysis of the change in thermocline feedback

As shown in Eq. (1), determining the change in thermocline feedback requires examining changes in four parameters. First, the DY+SH effects of the TP lead to an intensification of the mean upwelling in the equatorial eastern Pacific (Fig. 7d), which is dynamically consistent with the increased divergence of the mean meridional flow (Fig. 8d). The changes in the equatorial upwelling are largely driven by the DY effect of the TP (Figures 7e and 7f). Specifically, the response of the upwelling term $\langle \frac{\bar{w}}{H_1} \rangle_E$ to DY and SH forcing shows that the DY effect increases it by 24.2%, while the SH effect reduces it by 2.4% (Fig. 9c), further demonstrating that the dynamical process plays a dominant role in this variation.

Second, the combined DY+SH effects of the TP cause the regression coefficient

of sea surface height to wind stress (β_h) to exhibit a spatial distribution that is negative in the east and positive in the west (Fig. 10d), resulting in a negative east-west difference and an overall 34.9% reduction in β_h (Fig. 9c). This distribution pattern is primarily dominated by the DY effect (Fig. 10e), which individually contributes to a 39.9% reduction in β_h (Fig. 9c). In contrast, the SH effect exerts an opposite influence, increasing β_h by 8.3% (Fig. 9c), which is associated with the adjustment of the thermocline structure but remains relatively weak (Fig. 10f).

As discussed in previous studies (Hirst, 1986; An and Bong, 2016, 2018), β_h is inversely proportional to the mean thermocline depth and ocean stratification, represented by the expression: $\beta_h \approx \frac{L}{2\rho g' H}$. Where H represents the mean upper layer depth, ρ is ocean density, L is the zonal width of the Pacific Ocean at the equator, and g' is reduced gravity.

The DY+SH effects of the TP lead to a deepened mean thermocline and warming of the upper-layer waters (Fig. 7d), primarily due to the strengthened mean easterly winds in the equatorial eastern Pacific (Fig. 5d). The deepened thermocline weakens the sensitivity of the oceanic response to anomalous wind stress forcing, thereby reducing β_h. Simultaneously, the warming of the upper-layer waters strengthens the ocean stratification, further inhibiting the response capacity to surface zonal wind stress variations. Specifically, the warming reduces the water density (ρ) and increases the reduced gravity (g'), both of which lead to a decrease in β_h. Therefore, theoretical analysis also indicates that the reduction in β_h is the result of the combined effect of increased thermocline depth and enhanced ocean stratification.

Finally, the α_h factor decreased by approximately 4.3% in the presence of the TP. Although this reduction is small, it still indicates that the combined DY+SH effects of the TP weaken the sensitivity of the subsurface temperature to thermocline depth anomalies. The underlying mechanism is that the combined DY+SH effects enhance the stability of the vertical seawater stratification, thereby suppressing subsurface ocean temperature fluctuations.

In summary, the combined DY+SH effects of the TP reduce the thermocline feedback (TH) by 0.10 year^{-1}, accounting for approximately 18.0% of the total decrease in the BJ index. This variation is primarily caused by the balance between the reduction in β_h and the simultaneous increase in mean upwelling $\langle\frac{\overline{w}}{H_1}\rangle_E$ and atmospheric response sensitivity μ_a, with little change in α_h. Specifically, the DY effect weakens the thermocline feedback by controlling the significant decrease in β_h and the increase in both mean upwelling $\langle\frac{\overline{w}}{H_1}\rangle_E$ and the atmospheric response coefficient μ_a, while the contribution from α_h remains minor. From the perspective of individual forcing, the DY effect reduces the TH feedback by 0.21 year^{-1}, while the SH effect results in a reduction of 0.11 year^{-1}.

4.5 Analysis of Ekman feedback change

The combined DY+SH effects of the TP suppress the ENSO growth rate, with the weakening of the Ekman feedback term being a key factor (Figure 9b). This feedback depends on the air-sea coupling coefficients μ_a, the vertical flow response coefficient β_w, and the upper ocean stratification. Specifically, the combined DY+SH lead to a 33.3% reduction in β_w (Figure 9c). Further analysis of the response of the equatorial

Pacific vertical flow (w') to the zonal wind stress anomalies ($\tau_x^{'}$) revealed that under DY+SH forcing, a unit amount of easterly wind anomaly in the eastern equatorial Pacific leads to an intensification of the upwelling anomaly w' (Fig. 11d), indicating that the suppressing effect of upwelling on SST is weakened, i.e., the coupling between w' and $\tau_x^{'}$ is reduced (β_w decreases). This response is primarily dominated by the DY effect, which individually contributes to a 38% decrease in β_w (Fig. 11e); in contrast, the SH effect exhibits an opposite spatial distribution, resulting in a minor increase of 7.8% in β_w (Fig. 11f).

Second, the impact of the TP on the upper ocean stratification process $\langle -\frac{\partial \bar{T}}{\partial z} \rangle_E$ in the eastern equatorial Pacific is relatively small, weakening by only 3.6% (Figure 9c), and thus its contribution to the Ekman feedback is relatively small. The reduction in $\langle -\frac{\partial \bar{T}}{\partial z} \rangle_E$ in the eastern Pacific is mainly due to the cooling of the upper mixed layer being more significant than that of the deeper layers (Figure 7d). Concurrently, the aforementioned air-sea coupling coefficient μ_a increased by 16.6% under the combined thermal and dynamic forcing of the TP, which favors the intensification of the Ekman feedback (Fig. 9c).

Integrating the combined effects of these three parameters—the reductions in both the stratification gradient $\langle -\frac{\partial \bar{T}}{\partial z} \rangle_E$ and β_w, alongside the increase in μ_a—the net effect induced by the TP is a weakening of the Ekman feedback by 0.20 year^{-1}, accounting for approximately 40.0% of the total reduction in the BJ index. Specifically, the dynamic (DY) effect dominates the weakening of this feedback with a contribution of approximately −0.27 year^{-1}, whereas the thermal (SH) effect exerts an opposite

453 influence, strengthening the feedback by about +0.21 year^{-1}.

454 ## 4.6 Change of thermodynamic damping feedback

455 Thermodynamic feedback in the tropical Pacific is primarily derived from
456 shortwave radiation (α_{sw}) and latent heat flux (α_{lh}), while longwave radiation (α_{lw})
457 and sensible heat flux (α_{sh}) contribute less (Fig. 12a). Under the influence of the TP,
458 the thermodynamic damping (TD) feedback overall weakens by approximately 0.14
459 year−1, acting as the sole factor that increases the BJ index. This weakening primarily
460 stems from the enhancement of the shortwave radiation feedback (α_{sw}), which is
461 dominated by the dynamic effect (DY, contributing +0.43 year−1), while the thermal
462 effect (SH) partially offsets the impact of DY (contributing −0.29 year−1) (Fig. 12b).

463 The linear regression of tropical Pacific surface heat fluxes against the Niño 3.4
464 index (Fig. 13) reveals that the response of the surface net heat flux (α_{sw}) exhibits a
465 dipole pattern (negative in the east and positive in the west), consistent with the spatial
466 pattern of Walker circulation anomalies: the strengthened circulation reduces cloud
467 cover in the eastern Pacific, increasing shortwave absorption and partially offsetting the
468 damping effect of TD. This dipole variation is primarily driven by the DY effect (Fig.
469 13l), whereas the SH effect exhibits an anti-phase distribution, serving as a
470 counteracting factor (Fig. 13q). Furthermore, the latent heat flux (α_{lh}) shows a
471 meridional dipole distribution in the eastern tropical Pacific, resulting in a weak
472 contribution after regional averaging (Fig. 13m, r).

473 # 5. Discussions and conclusions

5.1 Discussions

This study explores the response of ENSO to the TP's topography and sensible heating, yet certain conclusions involve uncertainties that warrant further discussion. First, the impact of the sensible heat effect in the CMP and NSH experiments exhibits instability: The Niño 3.4 standard deviation in the CMP experiment is slightly stronger than that in NSH during the final 200 years (Fig. 1f). However, as ENSO activity in both experiments possesses multi-centennial oscillations with magnitudes comparable to the TP's sensible heat effect, the signals are easily masked by low-frequency oscillations, leading to uncertainty in the conclusion. Notably, previous research has indicated that the impacts of the TP's thermal and dynamic effects on large-scale monsoon circulation are nearly opposite (He et al., 2020), which indirectly supports our finding that the dynamic and thermal effects of the TP on ENSO activity also exhibit opposite signs, particularly regarding the thermodynamic feedbacks associated with atmospheric processes within the BJ framework.

Second, the model resolution employed in this study (T31 atmospheric resolution) is relatively coarse, resulting in an overall weakened simulated ENSO amplitude, with an annual mean standard deviation of approximately 0.7°C. In contrast, higher-resolution simulations based on CESM (e.g., Capotondi et al., 2020) show an ENSO standard deviation of up to approximately 2°C. This discrepancy is consistent with the systematic underestimation of ENSO variability at low resolutions: previous studies noted that the ENSO standard deviation at T31 resolution is generally below 1°C; for example, Li et al. (2024) simulated a pre-industrial ENSO variability of only about

0.6°C, and Shields et al. (2012) confirmed the weakened ENSO characteristics in this model resolution. It is worth emphasizing that although the absolute simulated ENSO amplitude is weaker than observations due to resolution constraints, the relative changes between different sensitivity experiments are dynamically self-consistent and reliable. Such comparative research under a consistent physical framework effectively offsets systematic model biases, accurately capturing the direct physical signals of TP topographic changes on the equatorial Pacific air-sea coupling system. Consequently, our conclusions regarding the TP's impact on ENSO involve a certain degree of model dependency, which requires future verification through higher-resolution simulations to confirm their reliability.

Finally, both previous studies and our simulations indicate that removing the TP topography leads to a significant weakening or even collapse of the Atlantic Meridional Overturning Circulation (AMOC) (Tong et al., 2025), raising the question of whether the AMOC serves as a mediator in the TP's impact on ENSO. By comparing the three experiments, we find that while the AMOC is in a collapsed state in both NSH and CNP experiments (Fig. 1e), ENSO activity in the equatorial Pacific displays distinct characteristics: ENSO remains highly active in the CNP experiment, whereas it is significantly suppressed in the NSH experiment where topography is retained (Fig. 1f). This comparison intuitively demonstrates that the differences in ENSO intensity are primarily driven by the direct topographic dynamical effect of the TP rather than being transmitted through changes in the AMOC state. Furthermore, from the NSH to the CMP experiment, although the AMOC recovers significantly from a collapsed state to

518 a normal level (approximately 18 Sv, see Fig. 1e), the corresponding increase in ENSO
519 amplitude is negligible (Fig. 1f), further confirming the limited regulatory role of
520 AMOC changes on ENSO variability. This effectively excludes the possibility of the
521 AMOC as a major mediating factor, further highlighting the direct dynamical
522 contribution of the TP's topography. Other numerical experiments provide supporting
523 evidence; for instance, in North Atlantic freshwater forcing experiments, AMOC
524 collapse did not significantly affect ENSO activity (Liu et al., 2023). Together, these
525 simulation evidences suggest that under different climatic backgrounds, the impact of
526 the TP on ENSO primarily stems from its direct dynamical effects.

527 ## 5.2 Conclusions

528 This study systematically investigates the impacts of the TP's dynamic and thermal
529 effects on ENSO activity based on three long-term integration experiments using the
530 CESM model. The results demonstrate that the TP significantly suppresses the ENSO
531 amplitude by 0.51 °C (−41%), in which the dynamic (DY) and thermal (SH) effects
532 contribute to a reduction of 0.58 °C (−46%) and an increase of 0.07 °C (5%),
533 respectively. BJ index analysis shows that the SH+DY effects of the TP reduce the index
534 by 0.50 $year^{-1}$, which is consistent with the weakening of the ENSO amplitude.
535 Specifically, the TP modulates ENSO activity by enhancing the mean advection (MA)
536 damping feedback (+0.33 $year^{-1}$), weakening the thermocline (TH) feedback (−0.09
537 $year^{-1}$), the Ekman (EK) feedback (−0.20 $year^{-1}$), and the zonal advective (ZA)
538 feedback (−0.02 $year^{-1}$), while reducing the thermodynamic damping (TD) feedback
539 (+0.14 $year^{-1}$). Across these feedbacks, the influence of the DY effect is consistently

stronger than that of the SH effect, and their contributions to the BJ index occur in opposite directions, indicating that the DY effect plays a dominant role while the SH effect primarily serves as an offsetting factor.

The TP's dynamic and thermal effects suppress ENSO-related oceanic dynamical feedback terms (TH, ZA, and EK), primarily stemming from large-scale atmospheric circulation adjustments, sea surface temperature structure variations, reduced sensitivity of the ocean response to wind stress, and changes in ocean circulation and stratification. Specifically, the enhancement of MA damping feedback is associated with the strengthened trade winds and the resulting changes in zonal and meridional flows. The weakening of TH, EK, and ZA feedbacks corresponds to the reduction in sensitive parameters β_h, β_w and β_u, respectively. Furthermore, the reduction in TD damping feedback induced by the TP is closely linked to the increased shortwave radiation feedback (α_{sw}) resulting from the strengthened Walker circulation.

Funding This work was supported by the National Key R&D Program of China (Grant 2022YFF0801603), the Science and Technology Development Fund of CAMS (Grant 2026KJ002), and the Major science and technology project of the Xizang Autonomous Region (XZ202402ZD0006). We thank for the technical support of the National Large Scientific and Technological Infrastructure “Earth System Numerical Simulation Facility” (https://cstr.cn/31134.02.EL).

Acknowledgements We are grateful to Dr. Jiang Zhu for kindly providing technical support and the necessary scripts for the calculations.

Author contributions Baohuang Su was responsible for designing and conducting experiments, processing simulation results, creating figures, and drafting the manuscript. Yong Sun contributed to the research design and conceptualization, and offered feedback on drafts of the manuscript. ShuangZe Han and Na Wang engaged in discussions, refined the language, and provided comments on earlier versions of the manuscript.

Data availability The CESM version 1.2.2 is available from https://github.com/ESCOMP/CESM. The sensitivity simulation data for the dynamic and thermal effects of the Tibetan Plateau utilized in this ENSO analysis, which includes CMP, CNP, and NSH, is accessible by contacting S.B.

Ethics declarations

Conflict of interest The authors declare that they have no conflict of interest.

References

An SI, Bong H (2016) Inter-decadal change in El Niño-Southern Oscillation examined with Bjerknes stability index analysis. Clim Dyn 47:967–979.

An SI, Bong H (2018) Feedback process responsible for the suppression of ENSO activity during the mid-Holocene. Theor Appl Climatol 132:779–790.

Barnett TP, Dümenil L, Schlese U, Roeckner E, Latif M (1989) The effect of Eurasian snow cover on regional and global climate variations. J Atmos Sci 46:661–686.

Blackmon ML, Branstator GW, Bates GT, Geisler JE (1987) An analysis of equatorial Pacific sea surface temperature anomaly experiments in general circulation models with and without mountains. J Atmos Sci 44:1828–1844.

Boos WR, Kuang Z (2010) Dominant control of the South Asian monsoon by orographic insulation versus plateau heating. Nature 463:218–222.

585 Capotondi A, Deser C, Phillips AS et al (2020) ENSO and Pacific decadal variability in the
586 Community Earth System Model version 2. J Adv Model Earth Syst 12:e2019MS002022
587 Chen LX, Li W, Zhao P (2001) Impact of winter thermal condition of the Tibetan Plateau on the
588 zonal wind anomaly over equatorial Pacific. Sci China Ser D: Earth Sci 44:400–409.
589 Chen L, Zheng W, Braconnot P (2019) Towards understanding the suppressed ENSO activity during
590 mid-Holocene in PMIP2 and PMIP3 simulations. Clim Dyn 53:1095–1110.
591 DeWeaver E, Nigam S (1995) Influence of mountain ranges on the mid-latitude atmospheric
592 response to El Niño events. Nature 378:706–708.
593 Duan A, Wu G, Wang B, Turner AG, Hu J, Hu W, Zhang P, Hu D, Tang Y (2024) Drivers of East
594 Asian summer monsoon variability: Global oceans and the Tibetan Plateau. Sci Bull 69:2487–
595 2490.
596 Fedorov AV, Philander SG (2000) Is El Niño changing? Science 288:1997–2002.
597 Harrison TM, Copeland P, Kidd W, Yin A (1992) Raising Tibet. Science 255:1663–1670.
598 He B, Liu Y, Wu G, Bao Q, Zhou T, Wu X, Wang L, Li J, Wang X, Li J, Hu W, Zhang X, Sheng C,
599 Tang Y (2020) CAS FGOALS-f3-L model datasets for CMIP6 GMMIP Tier-1 and Tier-3
600 experiments. Adv Atmos Sci 37:18-28.
601 Hirst AC (1986) Unstable and damped equatorial modes in simple coupled ocean-atmosphere
602 models. J Atmos Sci 43:606–632.
603 Hu J, Duan A (2015) Relative contributions of the Tibetan Plateau thermal forcing and the Indian
604 Ocean sea surface temperature basin mode to the interannual variability of the East Asian
605 summer monsoon. Clim Dyn 45:2697–2711.
606 Huang J, Zhou X, Wu G, Xu X, Zhao Q, Liu Y, Duan A, Xie Y, Ma Y, Zhao P, Yang S, Yang K, Yang
607 H, Bian J, Fu Y, Ge J, Liu Y, Wu Q, Yu H, Wang B, Bao Q, Qie K (2023) Global climate impacts
608 of land-surface and atmospheric processes over the Tibetan Plateau. Rev Geophys
609 61:e2022RG000771.
610 Hurrell JW, Holland MM, Gent PR, Ghan S, Kay JE, Kushner PJ, Lamarque J, Large WG, Lawrence
611 DM, Lindsay K, Lipscomb WH, Long MC, Mahowald NM, Marsh DR, Neale R, Rasch PJ,
612 Vavrus S, Vertenstein M, Bader DC, Collins WD, Hack JJ, Kiehl JT, Marshall SJ (2013) The
613 Community Earth System Model: a framework for collaborative research. Bull Am Meteorol
614 Soc 94:1339–1360.

615 Jin FF (1997) An equatorial ocean recharge paradigm for ENSO. Part I: Conceptual model. J Atmos
616 Sci 54:811–829.
617 Kitoh A (2007) ENSO modulation by mountain uplift. Clim Dyn 28:781–796.
618 Krishnan R, Venkatesan C, Keshavamurty RN (1998) Dynamics of upper tropospheric stationary
619 wave anomalies induced by ENSO during the northern summer, a GCM study. Proc Indian
620 Acad Sci Earth Planet Sci 107:65–90.
621 Li X, Hu S, Hu Y et al (2024) Persistently active El Niño–Southern Oscillation since the Mesozoic.
622 Proc Natl Acad Sci USA 121:e2404758121
623 Liu W, Duarte Cavalcante Pinto D, Fedorov A et al (2023) The impacts of a weakened Atlantic
624 meridional overturning circulation on ENSO in a warmer climate. Geophys Res Lett
625 50:e2023GL103025
626 Manucharyan GE, Fedorov AV (2014) Robust ENSO across a wide range of climate. J Clim
627 27:5836–5850.
628 Molnar P, Boos WR, Battisti DS (2010) Orographic controls on climate and paleoclimate of Asia:
629 thermal and mechanical roles for the Tibetan Plateau. Annu Rev Earth Planet Sci 38:77–102.
630 Naiman Z, Goodman PJ, Krasting JP, Malyshev SL, Russell JL, Stouffer RJ, Wittenberg AT (2017)
631 Impact of mountains on tropical circulation in two earth system models. J Clim 30:4149–4163.
632 Nan S, Zhao P, Yang S, Chen J (2009) Springtime tropospheric temperature over the Tibetan Plateau
633 and evolutions of the tropical Pacific SST. J Geophys Res Atmos 114:D10104.
634 Nigam S, DeWeaver E (1998) Influence of orography on the extratropical response to El Niño events.
635 J Clim 11:716–733.
636 Ren X, Liu W (2025) Distinct anthropogenic aerosol and greenhouse gas effects on El
637 Niño/Southern Oscillation variability. Commun Earth Environ 6:24.
638 http://doi.org/10.1038/s43247-025-01996-w
639 Shaman J, Tziperman E (2005) The effect of ENSO on Tibetan Plateau snow depth: A stationary
640 wave teleconnection mechanism and implications for the South Asian monsoons. J Clim
641 18:2067–2079.
642 Shields CA, Bailey DA, Danabasoglu G, Jochum M, Kiehl JT, Levis S, Park S (2012) The low-
643 resolution CCSM4. J Clim 25:3993–4014.
644 Siuts T, Bayr T, Lübbecke JF (2023) Changes in ENSO characteristics in model simulations with

considerably altered background climate states. J Clim 36:467–483.

Su B, Jiang D, Zhang R, Sepulchre P, Ramstein G (2018) Difference between the North Atlantic and Pacific meridional overturning circulation in response to the uplift of the Tibetan Plateau. Clim Past 14:751–762.

Tang S, Piao S, Cai W et al (2025) Tropical Pacific zonal temperature gradient intensified by the Tibetan Plateau surface darkening. Geophys Res Lett 52:e2025GL117253.

Tong M, Yang H, Jiang R et al (2025) Pivotal role of Tibetan Plateau and Antarctic in shaping present-day Atlantic Meridional Overturning Circulation. J Clim 38:2239–2252

Wen Q, Döös K, Lu Z, Han Z, Yang H (2020) Investigating the role of the Tibetan Plateau in ENSO variability. J Clim 33:4835–4852.

Wu A, Ni Y (1997) The influence of Tibetan Plateau on the interannual variability of Asian monsoon. Adv Atmos Sci 14:491–504.

Wu G, Liu Y, He B, Bao Q, Duan A, Jin FF (2012) Thermal controls on the Asian summer monsoon. Sci Rep 2:404.

Wu Z, Li J, Jiang Z, Ma T (2012) Modulation of the Tibetan Plateau snow cover on the ENSO teleconnections: From the East Asian summer monsoon perspective. J Clim 25:2481–2489.

Yu W, Liu Y, Xu L, Wu G, Yang S, Chen D, Yang X-Q, Hu C, He B (2022) Potential impact of spring thermal forcing over the Tibetan Plateau on the following winter El Niño–Southern Oscillation. Geophys Res Lett 49:e2021GL097234.

Zhou X, Zhao P, Chen J, Chen L, Li W (2009) Impacts of thermodynamic processes over the Tibetan Plateau on the Northern Hemispheric climate. Sci China Ser D: Earth Sci 52:1679–1693.

666 Table 1. Parameters employed in the BJ index.

Terms	descriptions
$L_x,\ L_y$	Longitudinal and latitudinal length of the eastern box
H_1	Mixed layer depth
μ_a	Wind stress response to sea surface temperature (SST)
β_u	Zonal current response to wind
β_w	Upwelling response to wind
β_h	Zonal slope of thermocline depth response to wind stress
α_h	Subsurface temperature response to thermocline depth
α_s	Net surface heat flux anomaly response to SSTA anomalies

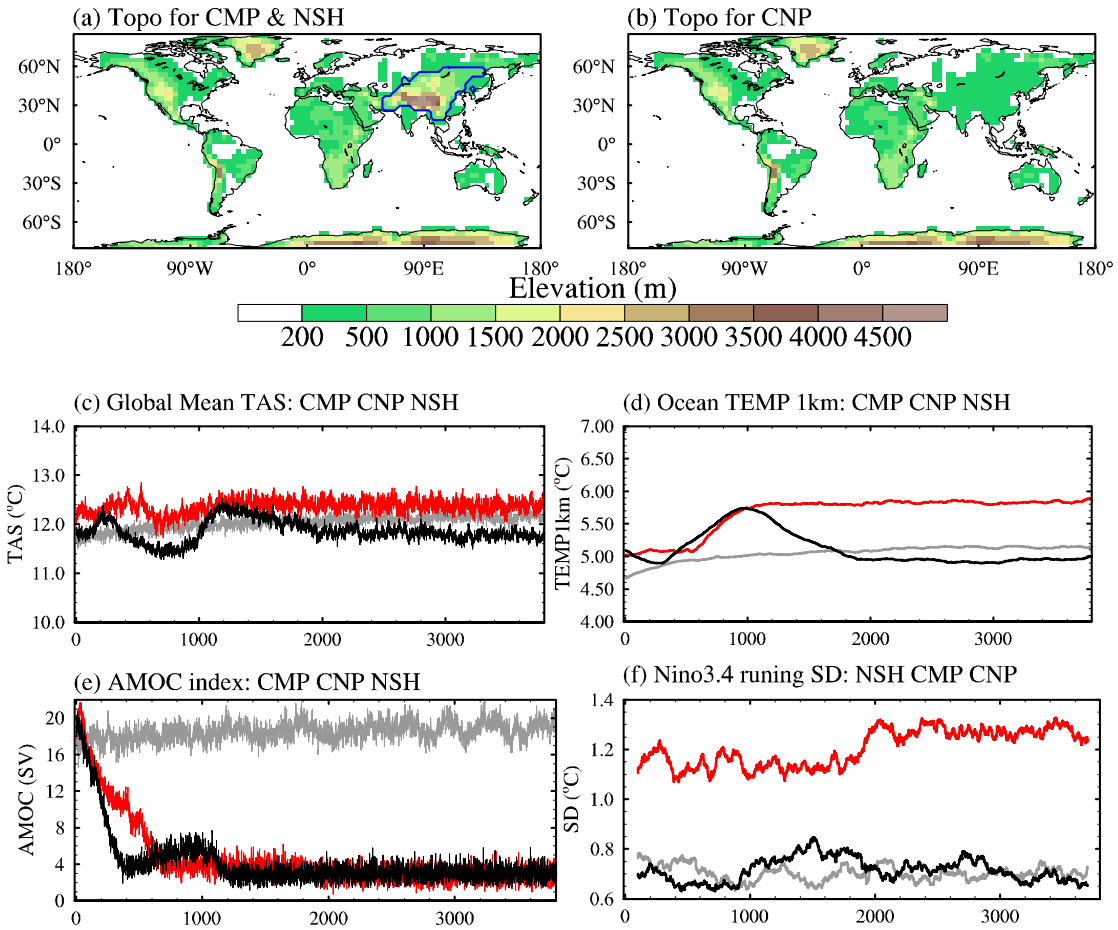

667

668 Figure 1 presents the TP height configuration and the stability of simulation runs: (a) Modern TP
669 height used in CMP and NSH (units: m), with blue contour lines indicating the sensible heat removal
670 region in NSH; (b) Topographic boundary conditions used in CNP (units: m); (c) Global annual
671 average 2-meter air temperature (TAS, units: °C); (d) Deep ocean temperature at 1000 m depth
672 (units: °C); (e) Atlantic Meridional Overturning Circulation (AMOC) index (units: Sv); and (f) 200-
673 year running standard deviation (STD) of the Niño 3.4 index (units: °C). Gray, black, and red lines
674 represent the CMP, NSH, and CNP experiments, respectively.

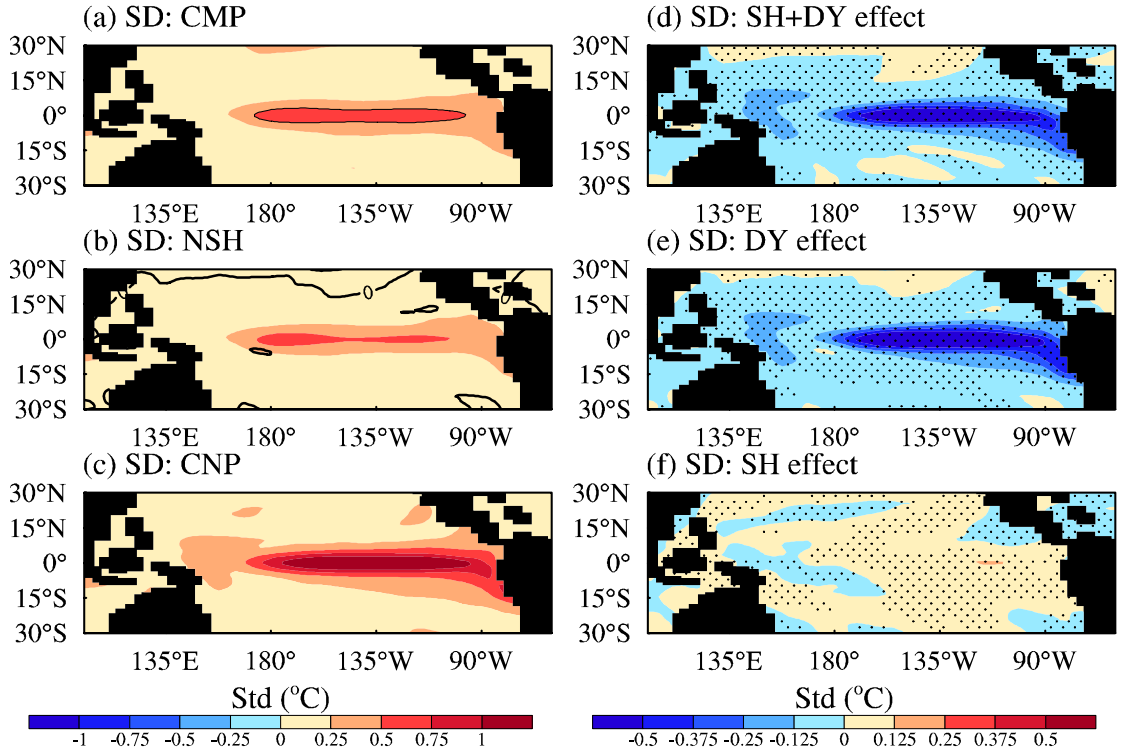

Figure 2 shows the standard deviation (STD, units: °C) of the the 2-7-year band-pass filtered sea surface temperature anomalies (SSTAs, with the annual cycle removed) in the tropical Pacific for the all experiments: (a) CMP, (b) NSH, and (c) CNP, each showing the climatological distribution of the three experiments. (d) shows the difference between CMP and CNP, representing the combined effects of the thermal and dynamic (DY+SH) effects of the TP; (e) shows the difference between NSH and CNP, representing the dynamic effect (DY); (f) shows the difference between CMP and NSH, representing the thermal effect (SH) of the TP. Stippled areas in (d–f) denote differences significant at the 99% confidence level.

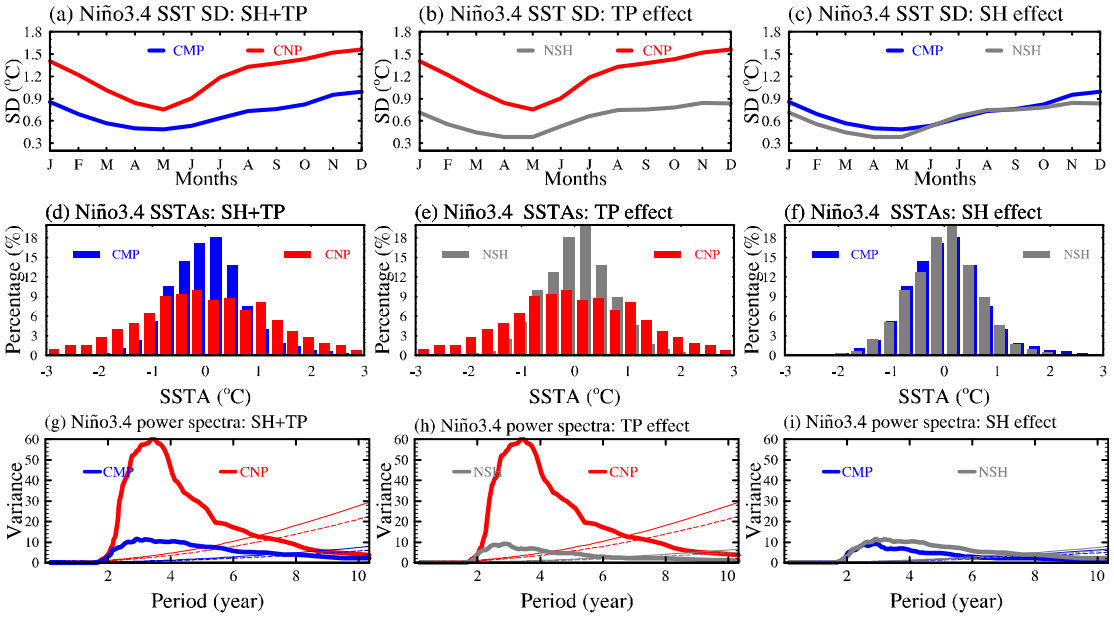

Figure 3 presents the statistical characteristics of monthly mean SSTAs (annual cycle removed) over a 200-model-year period: (a–c) Annual cycle of SSTA STD (units: °C), (d–f) Probability density distribution of Niño3.4 SSTAs (units: %), and (g–i) Power spectral density of SSTAs (units: $°C^2$), filtered for the 2–7-year band. In (g–i), light solid line indicate the 95% confidence level and the dashed line represents red noise spectrum. The plots are presented by comparing two experiments at a time to visually display the climatic effects of the TP.

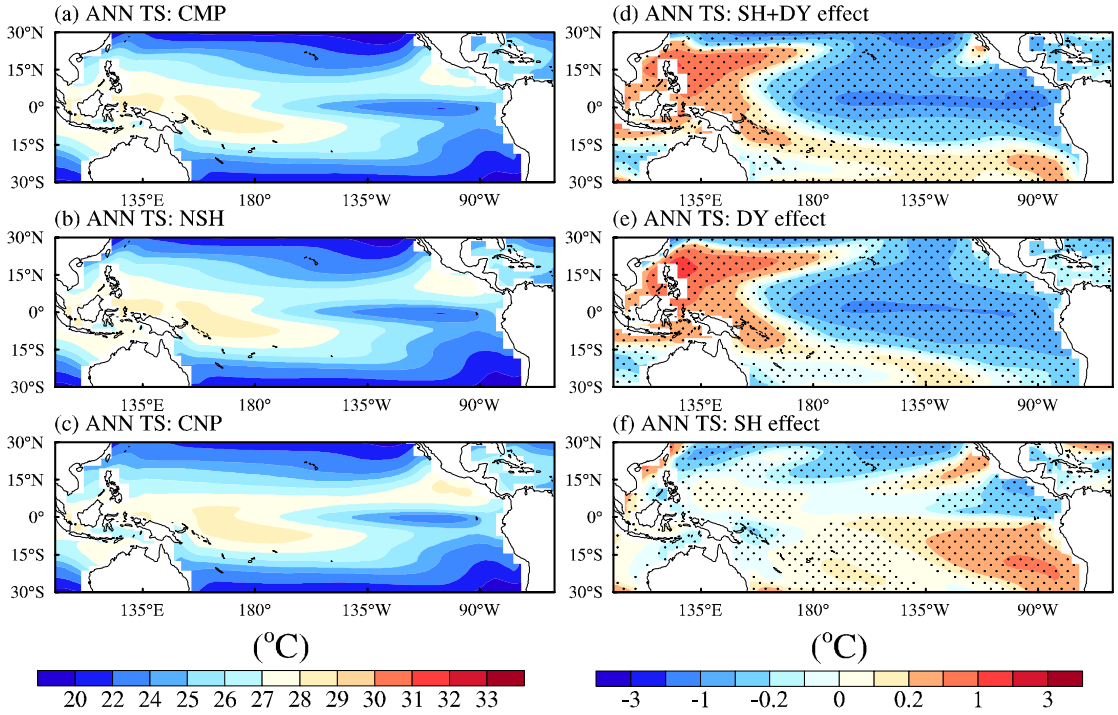

691

692 Figure 4 shows the climatological mean SST (units: °C) in the tropical Pacific for: (a) CMP, (b)

693 NSH, and (c) CNP. Differences represent (d) DY+SH effects, (e) individual DY effect, and (f)

694 individual SH effect. Stippled areas in (d–f) indicate differences passing the 99% confidence level.

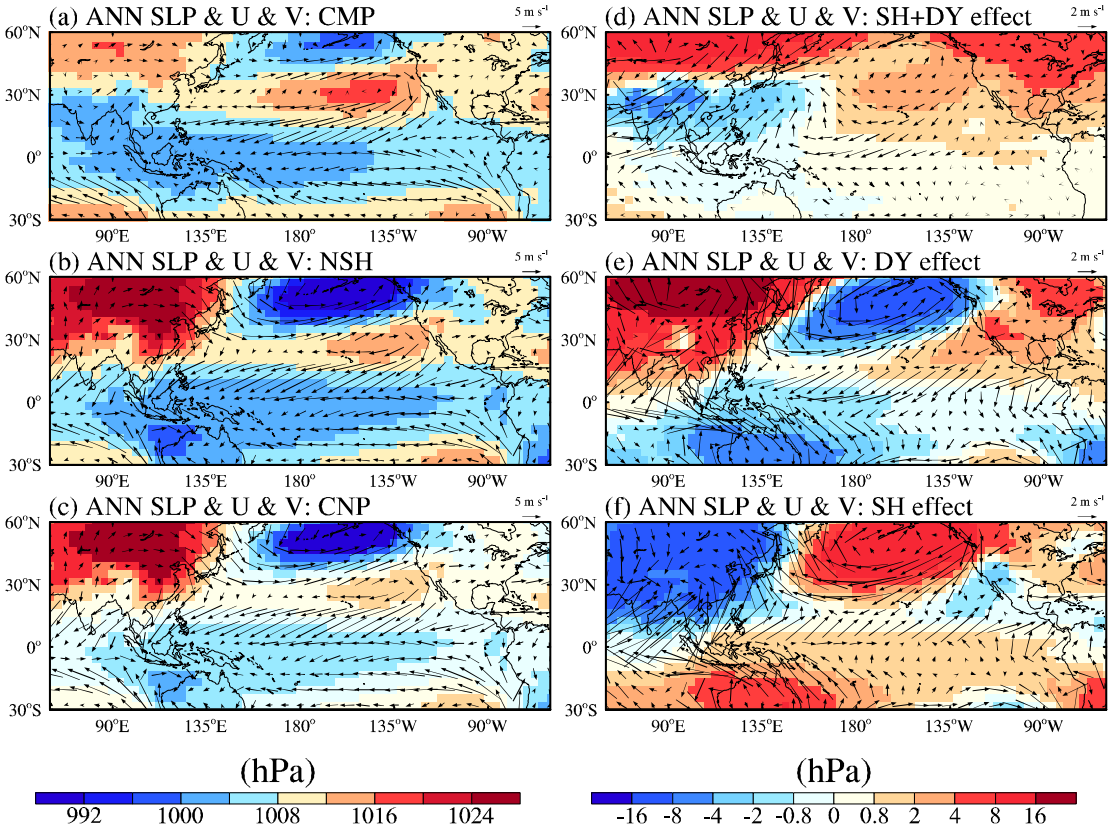

Figure 5: Same as Figure 4, but showing the simulated annual mean near-surface winds (vectors, units: m s^{-1}) and sea level pressure (shading, units: hPa) along with their anomalies.

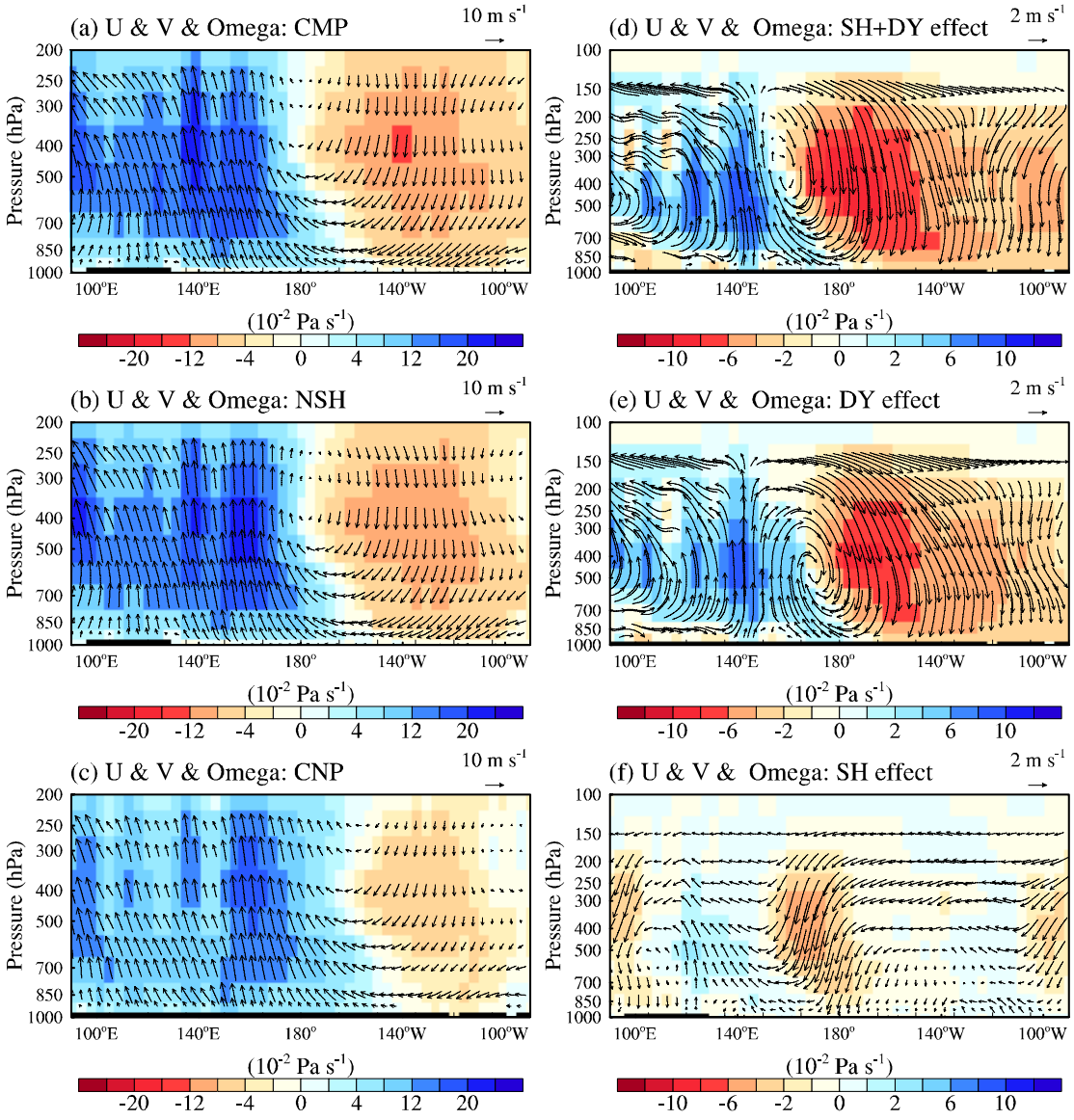

Figure 6 presents the annual mean climatological distribution and anomalies of the zonal circulation averaged between 5°S and 5°N. Vectors denote the zonal wind (m s^{-1}) and the vertical velocity (Pa s^{-1}); Shading indicates vertical velocity (positive for upward motion). Panels (a) CMP, (b) NSH, and (c) CNP show the mean states; (d) CMP−CNP, (e) NSH−CNP, and (f) CMP−NSH reveal the combined DY+SH, the individual DY, and the individual SH effects, respectively.

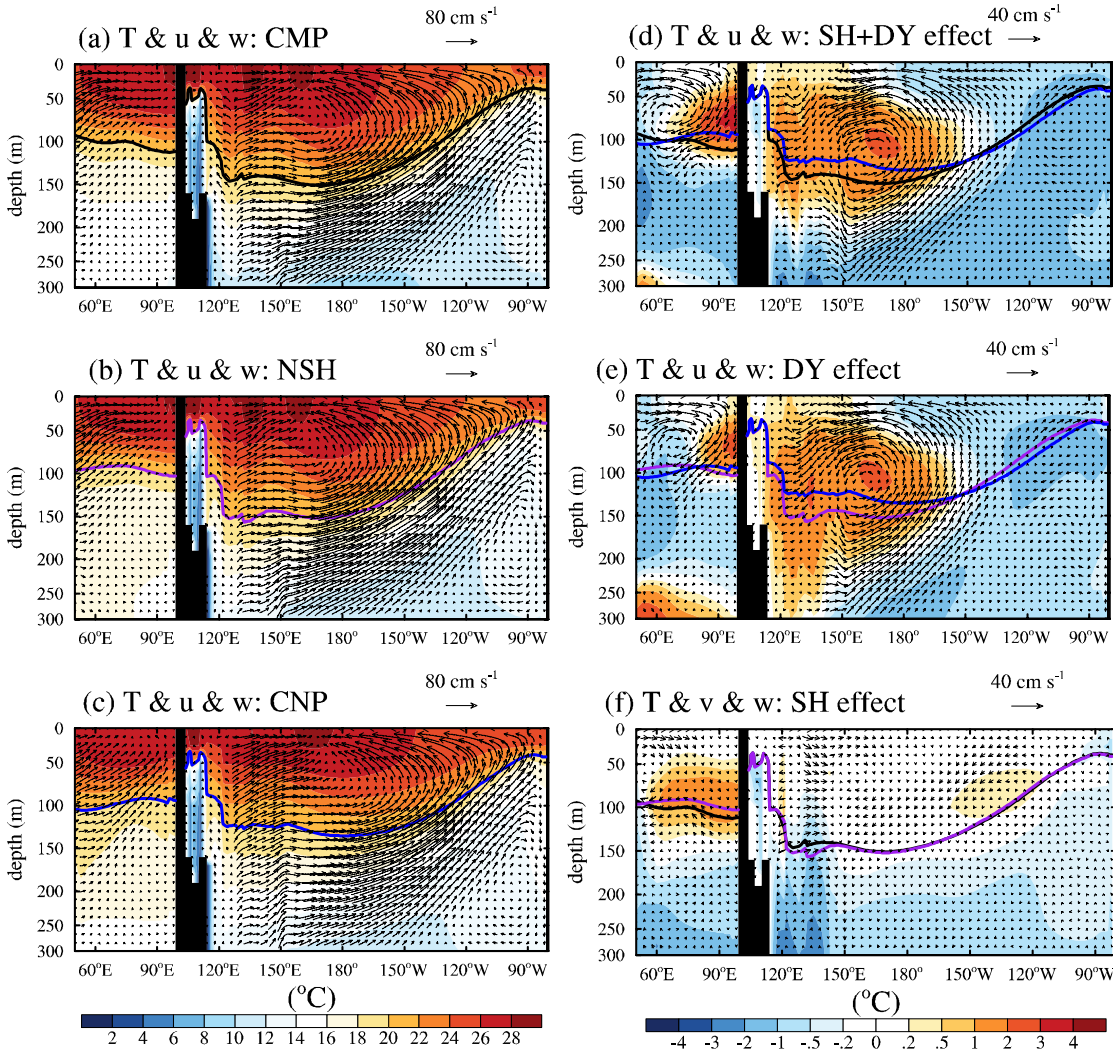

Figure 7 displays the annual mean zonal-vertical section of ocean circulation and temperature in the equatorial band (5°S–5°N): zonal velocity (vectors, units: cm s^{-1}), vertical velocity (units: 3.5 × 10^{-2} cm s^{-1}), and sea temperature (shading, units: °C). Differences represent the combined DY+SH, the DY effect, and the SH effect. Black, purple, and blue thick contours denote the 20 °C isotherms (thermocline depth) for CMP, NSH, and CNP, respectively.

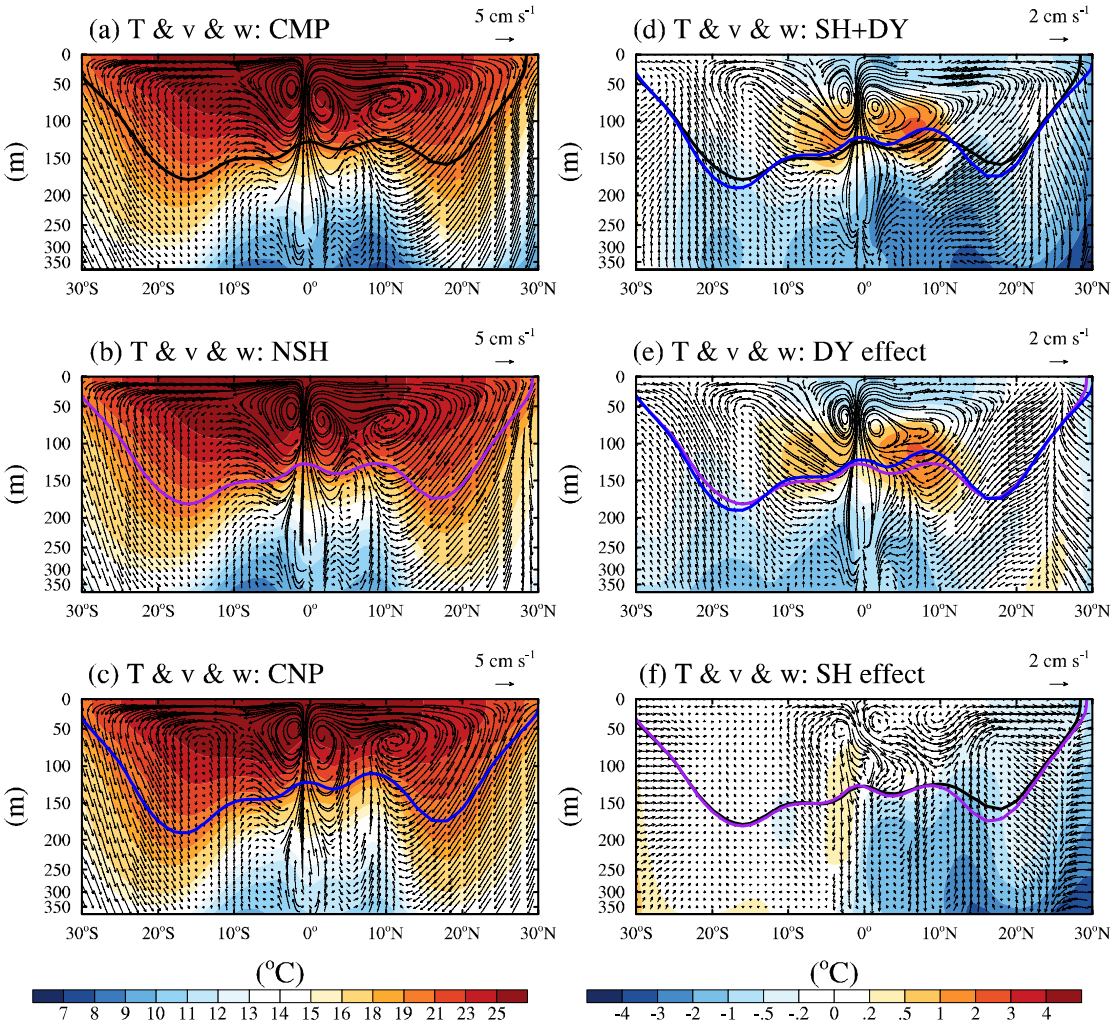

710

711 Figure 8: Same as Figure 7, but showing the simulated annual mean meridional-vertical section of
712 ocean circulation climatology (vectors; meridional velocity units: cm s^{-1}, vertical velocity units: 3.5
713 × 10^{-2} cm s^{-1}) and sea temperature (shading, units: °C), both averaged between 180° and 150°W.
714 Panels (a) CMP, (b) NSH, and (c) CNP show the mean states; (d–f) show the differences for DY+SH,
715 the individual DY, and the individual SH effects. Black, purple, and blue thick contours represent
716 the 20 °C isotherms for CMP, NSH, and CNP, respectively.

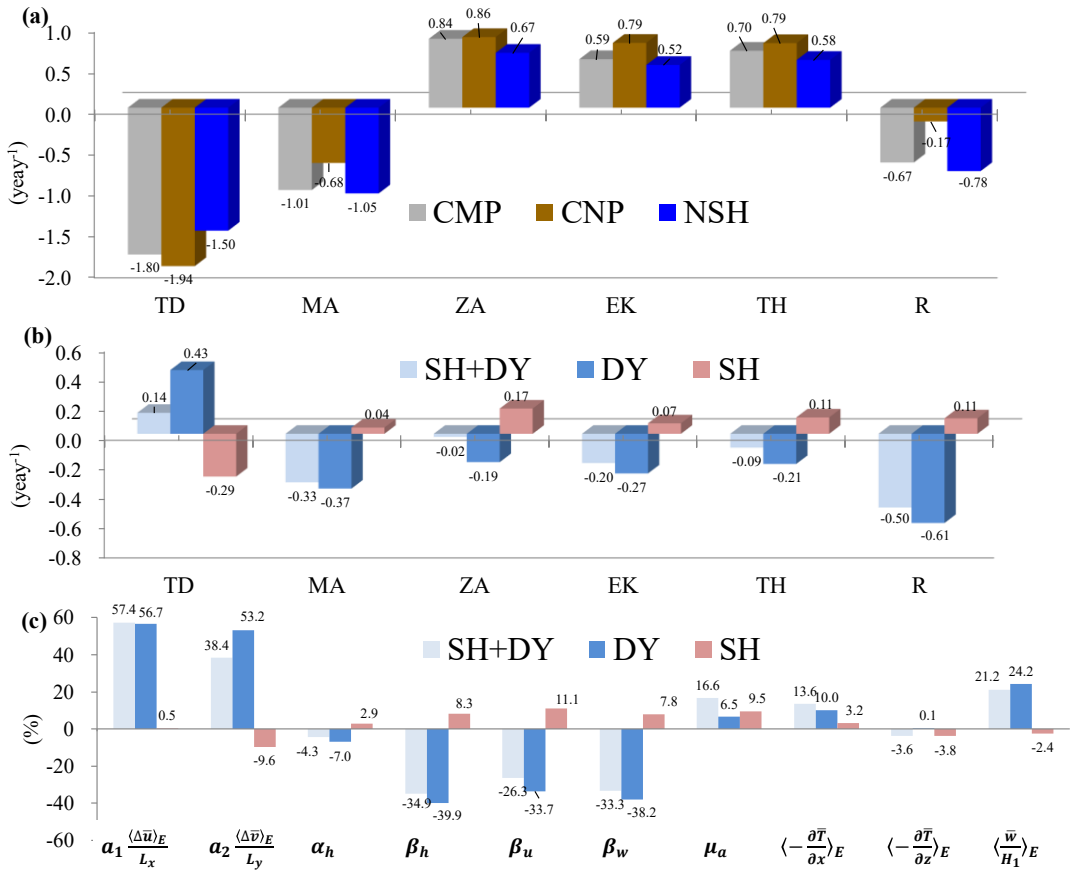

Figure 9 presents the calculated Bjerknes coupled stability index (BJ index, units: year^{-1}) and its five contributing factors for all experiments: (a) Values for CMP, NSH, and CNP. MA: mean advection feedback; TD: thermodynamic damping; ZA: zonal advective feedback; TH: thermocline feedback; and EK: Ekman feedback. (b) Impact of the combined DY+SH, the individual DY, and the individual SH effects on the index and its feedbacks. (c) Percentage changes in BJ index parameters in response to DY+SH, DY, and SH (units: %). Refer to Table 1 for parameter definitions.

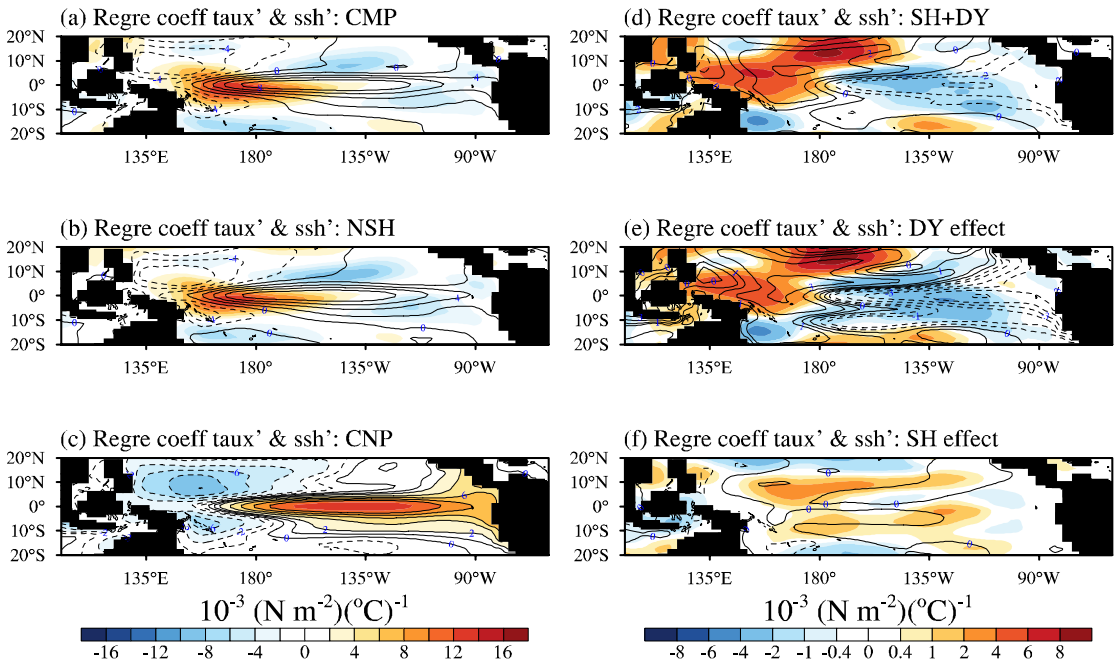

724

725 Figure 10 presents the regression coefficients of zonal wind stress anomalies ($\tau_x^{'}$) onto Niño 3.4

726 SSTAs (μ_a, shading) and the response of thermocline depth anomalies (using sea surface height

727 anomalies as a proxy) to $\tau_x^{'}$ (β_h, contours, units: m (N m^{-2})$^{-1}$). Panels (a–c) show mean states; (d–

728 f) show the impact of the combined DY+SH, the individual DY, and the individual SH effects.

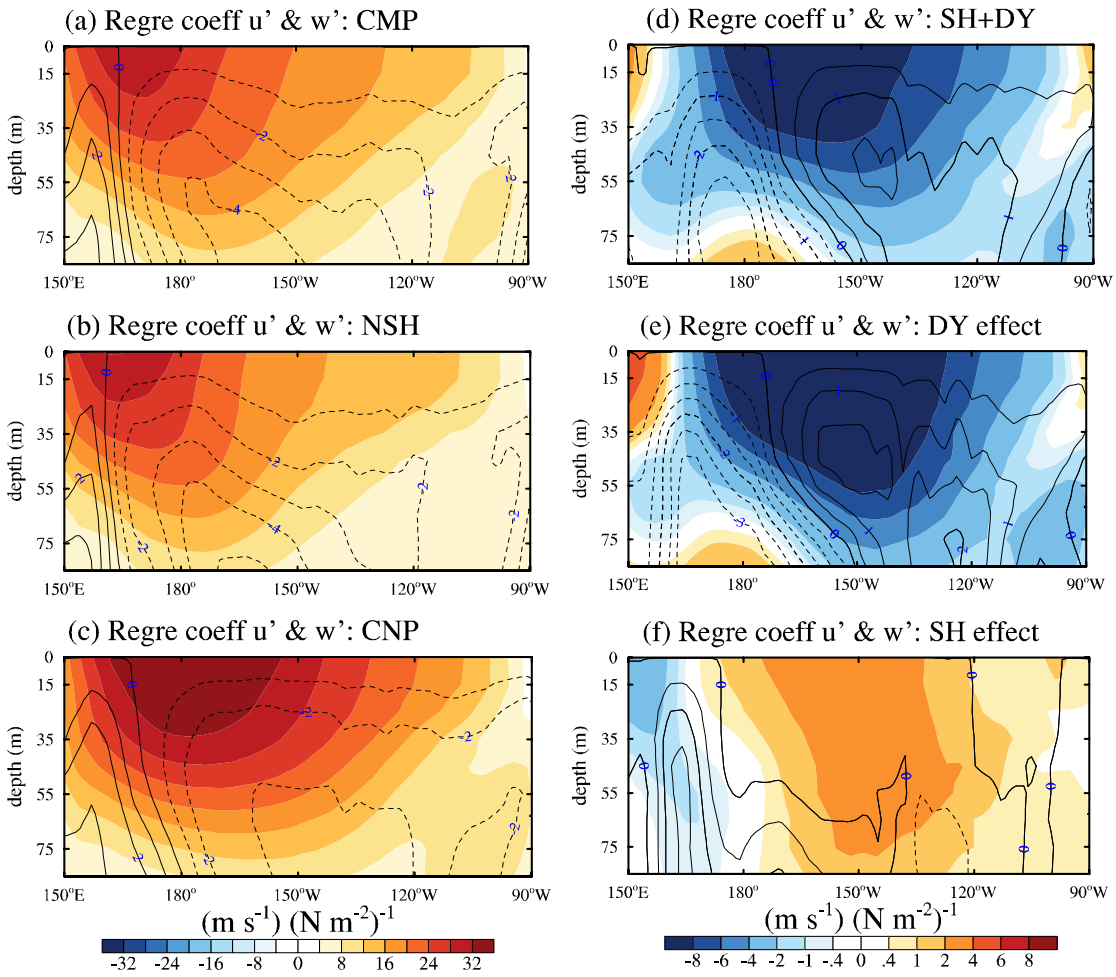

Figure 11 presents the vertical-zonal cross-sectional plots of zonal (u', shading) and vertical (w', contours) current anomalies along the equator (averaged 5°S–5°N) regressed onto τ_x'. Panels (a–c) show mean states; (d–f) show the impact of the combined DY+SH, the individual DY, and the individual SH effects. Contour intervals are 1.5×10^{-5} (m s^{-1}) (N m^{-2})$^{-1}$; solid (dashed) lines denote upward (downward) currents.

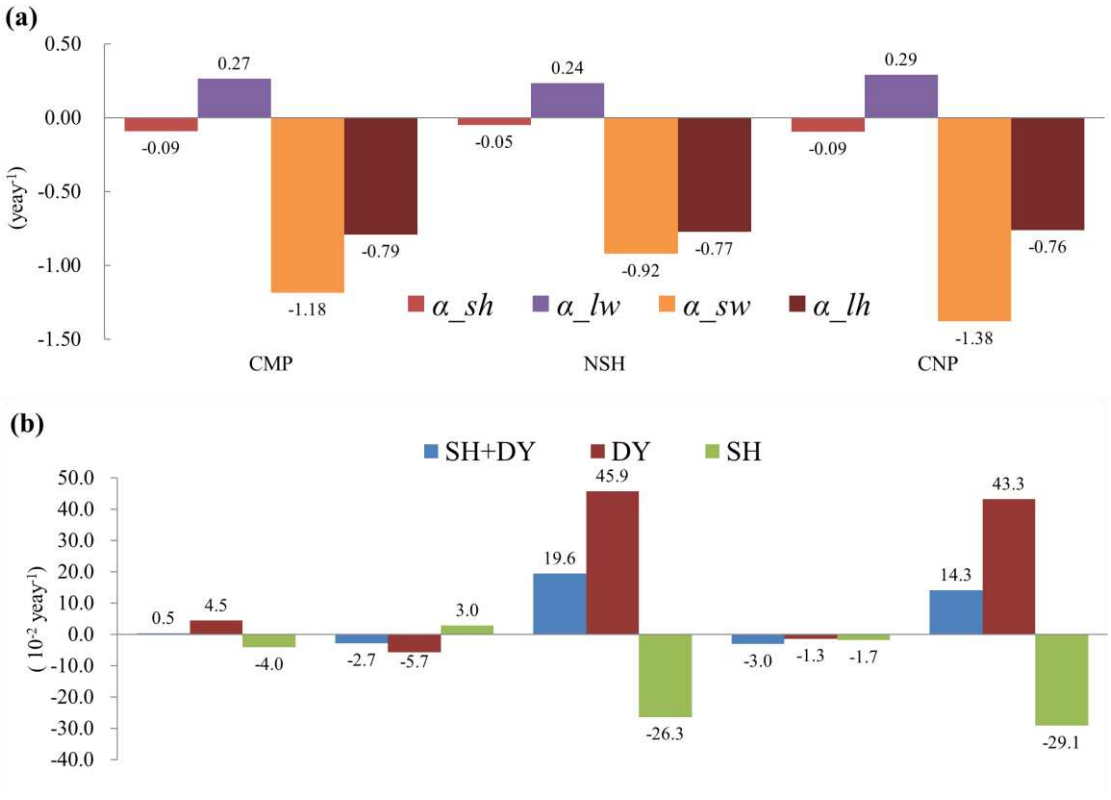

735

736 Figure 12: (a) Distribution of the four thermodynamic feedback components and total

737 thermodynamic damping for the three experiments. α_{sh}, α_{lw}, α_{sw}, and α_{lh} represent sensible

738 heat, longwave radiation, shortwave radiation, and latent heat feedback, respectively (units: year^{-1}).

739 (b) Impact of the combined DY+SH, the individual DY, and the individual SH effects on these

740 components and their net contribution to the total damping.

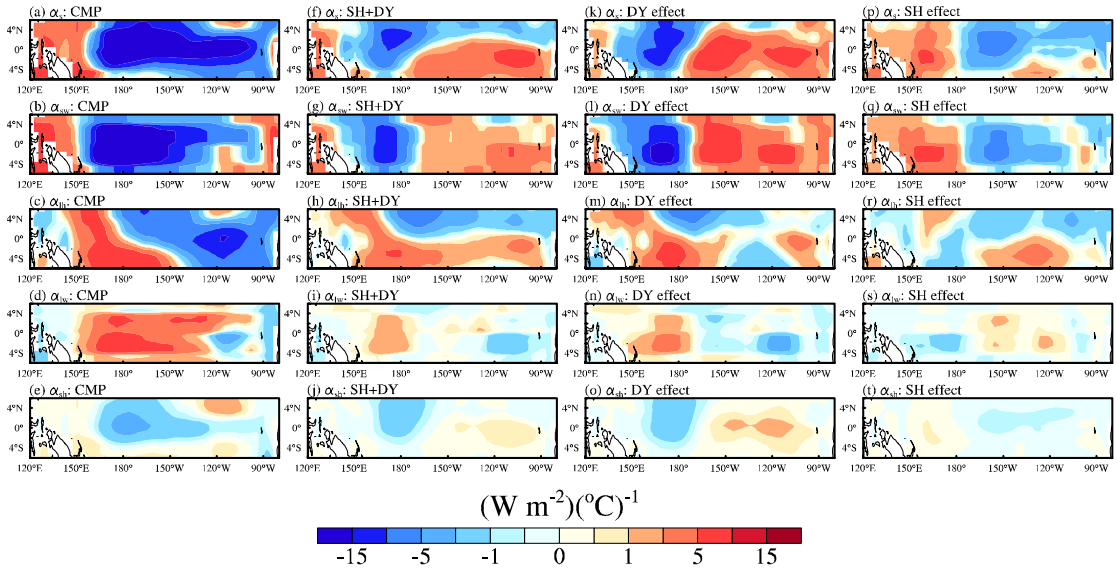

741

742 Figure 13 displays the spatial distribution of regression coefficients (units: W m^{-2} $°C^{-1}$) of tropical
743 sea surface heat flux anomalies against equatorial Pacific SSTAs in the equatorial Pacific region
744 (120°E–80°W, 5°N–5°S). Column 1 (a–e): CMP climatological distribution for net heat flux, net
745 shortwave radiation, latent heat flux, net longwave radiation, and sensible heat flux. Columns 2–4
746 (f–t): Impact of DY+SH effects, individual DY effect, and individual SH effect, respectively.